

# Dissecting inertial clustering and sling dynamics in high-Reynolds number particle-laden turbulence

Lukas A. Codispoti,<sup>a)</sup> Daniel W. Meyer, and Patrick Jenny

*Institute of Fluid Dynamics, ETH Zürich, Sonneggstrasse 3, 8092 Zürich, Switzerland*

(Dated: 28 October 2024)

In this work, we aim to deepen the understanding of inertial clustering and the role of sling events in high-Reynolds number ( $Re$ ) particle-laden turbulence. To this end, we perform one-way coupled particle tracking in flow fields obtained from direct numerical simulations (DNS) of forced homogeneous isotropic turbulence. Additionally, we examine the impact of filtering utilized in large eddy simulations (LES) by applying a sharp spectral filter to the DNS fields. Our analysis reveals that while instantaneous clustering through the centrifuge mechanism explains clustering at early times, the path history effect—the sampling of fluid flow along particle trajectories—becomes important later on. The filtered fields expose small-scale fractal clustering that cannot be predicted by the instantaneous flow field. We show that there exists a filter-effective Stokes number that governs the degree of fractal clustering and preferential sampling, revealing scale-similarity in the spatial distributions and fractal dimensions. Sling events are prevalent throughout our simulations and impose prominent patterns on the particle fields. In pursuit of investigating the sling dynamics, we compute the relative velocity, ensemble-averaged over proximal neighboring particles, to identify particles undergoing caustics. As postulated in recent theories, we find that in fully resolved, high- $Re$  turbulence, sling events occur in thin sheets of high strain, situated between turbulent vortices. This behavior is driven by rare, extreme events of compressive straining, manifested by fluctuations of the flow velocity gradients that propagate back and forth the positive branch of the Vieillefosse line.

## I. INTRODUCTION

Inertial particles detach from the flow and form clusters. This phenomenon is significant in a wide range of natural processes and engineering applications, e.g., the growth of droplets in atmospheric clouds<sup>1</sup>. Even in randomly-forced suspensions with a single characteristic timescale, intricate patterns of the density field can be observed<sup>2</sup>. At high Reynolds numbers, turbulent flows exhibit broad ranges of highly separate temporal and spatial scales with strong intermittency, especially at high wavenumbers. Clustering is then a complex, multiscale process, driven by multiple mechanisms. Particles cluster both by action of the instantaneous flow field and by the path-history effect, i.e., by collecting memory along their paths. The former is typically described as particles being centrifuged out of regions of high vorticity and accumulating in regions of high strain<sup>3,4</sup>. The latter produces fractal spatial distributions and leads to sling events, whereby the particle dynamics exhibits phase-space singularities, so-called caustics<sup>5–7</sup>, resulting in anomalous particle number density fields and large relative velocities. Caustics are said to play a key role in the collisions of droplets in clouds<sup>8,9</sup>, which initiate rainfall, offering a possible solution to the bottleneck problem of cloud physics<sup>10</sup>.

It is widely accepted (e.g., Refs. 11–13, to only name a few) that clustering is most intense when flow and particle timescales are comparable, i.e. when the Stokes number, defined as the ratio between particle relaxation to

the Kolmogorov timescale,  $St = \tau_p/\tau_\eta$ , is close to unity. This implies that the smallest scales of the flow are most relevant in explaining clustering. In this work, we investigate the effect of filtering the turbulent flow field, i.e., removing the smallest scales, on the mechanisms that drive particle clustering. This is highly relevant for LES of particle-laden turbulence, in which the Navier-Stokes equations are solved for a filtered, coarse-grained velocity field, leaving the sub-grid scales (SGS) unresolved. While this approach significantly lowers computational costs, it requires modeling to capture the influence of the unresolved scales. This poses a challenge, especially for particle-laden flows, where clustering is driven by the coherent motion at the smallest scales.

In this work, we assume dense point-particles of negligible spatial extensions in dilute suspensions, so that their motion can be approximated by<sup>7</sup>

$$\dot{\mathbf{x}} = \mathbf{v}, \quad \dot{\mathbf{v}} = \frac{\mathbf{u}(\mathbf{x}, t) - \mathbf{v}}{\tau_p}, \quad (1)$$

where  $\mathbf{x}$  and  $\mathbf{v}$  are the particle position and velocity, respectively, and  $\mathbf{u}(\mathbf{x}, t)$  is the local flow velocity. Equation (1) neglects particle-fluid and particle-particle interactions, which is commonly referred to as *one-way coupling*. The approach is convenient for DNS, since it separates the flow computation from the particle tracking and enables the study of clustering in isolation. If there exists a continuous, smooth velocity field that describes the motion of the particles,  $\mathbf{u}_p(\mathbf{x}, t)$ , then Eq. (1) can be written in the Eulerian frame of reference as

$$\frac{D_p \mathbf{u}_p}{Dt} := \frac{\partial \mathbf{u}_p}{\partial t} + (\mathbf{u}_p \cdot \nabla) \mathbf{u}_p = \frac{\mathbf{u} - \mathbf{u}_p}{\tau_p}. \quad (2)$$

Since  $\dot{\mathbf{v}}$  in Eq. (1) represents the substantial derivative

<sup>a)</sup>Electronic mail: lukasco@ethz.ch

of that particle velocity field along a particle path, i.e.,  $D_p \mathbf{u}_p / Dt$ , the particle number density  $n(\mathbf{x}, t)$  is a conserved scalar that is transported with  $\mathbf{u}_p$  and satisfies

$$\frac{D_p \ln n}{Dt} = -\nabla \cdot \mathbf{u}_p := -\xi, \quad (3)$$

which can be derived from the conservation equation  $\partial_t n + \nabla \cdot (n \mathbf{u}_p) = 0$ . The particle velocity divergence, herein after denoted by the symbol  $\xi$ , is an explicit source term on the right-hand side of Eq. (3). In other words, it is the compressibility of the particles which lag the incompressible flow that produces variance in  $n$ . From Eq. (2) we find that  $\xi$  evolves according to

$$\frac{D_p \xi}{Dt} = -\frac{\xi}{\tau_p} - \text{tr}(\mathbb{U}^2), \quad (4)$$

where  $\mathbb{U}_{ij} = \frac{\partial u_{p,i}}{\partial x_j}$  (and  $\xi = \text{tr}(\mathbb{U})$ ). As seen from Eq. (4), the particle velocity divergence relaxes at the rate  $\tau_p^{-1}$  towards zero, since the carrier fluid is incompressible, i.e.,  $\nabla \cdot \mathbf{u} = 0$ . The non-linear term on the right-hand side of Eq. (4) can, however, render the system unstable. This is a first indication that at large enough Stokes numbers the particle dynamics are susceptible to finite-time singularities, i.e., that  $\xi$  might escape to  $-\infty$  in finite time. In fact, as  $\tau_p \rightarrow \infty$ , Eq. (2) reduces to the three-dimensional (3D) inviscid Burgers equation, which is well-known for producing shocks resulting from gradient *self-amplification* of the convective term<sup>14</sup>. In the context of particle-laden flows, blow-up events of this kind are referred to as caustics, which will be discussed in more detail below.

Let us now turn to the mechanisms that drive inertial particles to cluster. Maxey<sup>3</sup> used the continuum approach and expressed for  $St \rightarrow 0$  the particle velocity field as  $\mathbf{u}_p = \mathbf{u} + \tau_p \frac{D\mathbf{u}}{Dt} + \mathcal{O}(\tau_p^2)$ . The particle velocity divergence then results from this limiting expression as

$$\xi \approx 2\tau_p Q. \quad (5)$$

Here,  $Q = -\frac{1}{2} \text{tr}(\mathbb{A}^2)$  is the second invariant of the flow velocity gradient (FVG) tensor  $\mathbb{A}_{ij} = \frac{\partial u_i}{\partial x_j}$ , expressing the difference between rotation and dissipation of the local flow topology<sup>14,15</sup>. Therefore, Eq. (5) indicates that particles tend to reside in regions where strain dominates vorticity, consistent with the notion of *Maxey's centrifuge*, according to which particles are ejected out of turbulent eddies and accumulate in areas of low vorticity. This mechanism, also referred to as *preferential sampling*, explains clustering purely based on the instantaneous flow field. Strictly speaking, it is only valid at small Stokes numbers, whereas higher order terms of the FVGs play a more significant role for heavier particles. As a particle's inertia increases, memory effects become more pronounced, and the history of  $\mathbb{A}$  sampled along its trajectory exerts greater influence on its instantaneous velocity.

Aside from Maxey's centrifuge, the clustering of inertial particles in turbulence is indicative of the dissipative dynamics governed by Eq. (1), which evolve towards a fractal phase-space attractor<sup>2,16,17</sup>. This means that particles cluster onto fractal sets in physical space in the smallest scales of the flow, i.e., at lengths  $\ell \sim 10\eta$ . The fractal dimension, which quantifies the 'space-fillingness' of the particle distribution, depends on the Stokes number and has significant implications for processes such as collision, evaporation or condensation of droplets in turbulence. Fractal patterns have been observed in particle-laden simulations with synthetic as well as fully-resolved turbulence and are commonly quantified with the correlation dimension<sup>17</sup>,  $d_2$ . If  $N(r)$  is the number of neighbors a particle is surrounded by inside the sphere of radius  $r$ , then<sup>7</sup>  $N(r) \sim r^{d_2}$ . In 3D configuration space, fractal particle clusters are characterized by  $d_2 < 3$ . While preferential sampling is still relevant in the small scales<sup>12</sup>, the history of the FVGs that particles sample along their paths must be taken into account in order to explain fractal clustering. Here, it is appropriate to move away from Eq. (4), which describes the evolution of the divergence of the *synthetic*, continuous particle velocity field, and instead study the evolution of the Lagrangian particle velocity gradient tensor,  $\mathbb{Z}_{ij} = \frac{\partial v_i}{\partial x_j}$ , given by<sup>5,7,17</sup>

$$\dot{\mathbb{Z}} = \frac{\mathbb{A} - \mathbb{Z}}{\tau_p} - \mathbb{Z}^2. \quad (6)$$

Note that Eq. (4) corresponds to the trace of Eq. (6) in the Eulerian frame of reference. By studying Eq. (6), however, we depart from the restricting assumption of a continuous particle velocity field and directly observe the effect of the FVGs, which vanishes when applying the trace operator due to incompressibility. The path-history effect gives rise to *multiplicative amplification*<sup>7</sup>, referring to the mechanism by which the volumes spanned by small particle clouds randomly contract and expand. The rate of contraction/expansion as well as the spatial Lyapunov exponents of the system can be expressed using  $\text{tr}(\mathbb{Z})$ .

The mechanism that has received arguably the most attention lately<sup>18-23</sup> is clustering by caustics, which are singularities in the dynamics of  $\mathbb{Z}$ . As inertial particles experience individual histories of flow velocity (gradients) along their trajectories, which influence their instantaneous state, multiple particles with different velocities can occupy the same positions in time and space. This phenomenon was termed *sling effect* by Falkovich *et al.*<sup>5</sup>, and the phase-space singularity required for it to occur became known as a *caustic*<sup>6</sup>, named after the patterns that light casts onto the bottom of a body of water on a sunny day. A caustic is a blow up of Eq. (6), corresponding to  $\text{tr}(\mathbb{Z}) \rightarrow -\infty$ . When it occurs, the phase space folds, and the singularity in the particle velocity divergence leads to multivalued particle velocities and extreme local increases in the particle number density.

To illustrate the physical phenomenon of the caustic, let us consider a simple, one-dimensional setting. Here,



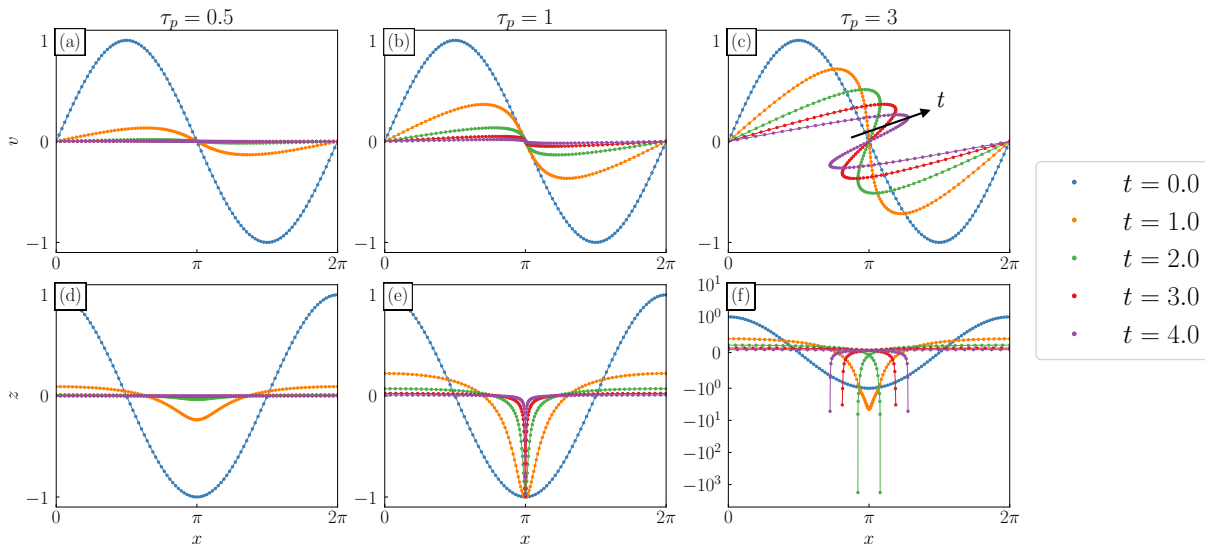


**FIG. 1:** Caustic formation in a one-dimensional model problem. Solution to (a-c) Eq. (7) and (d-f) Eq. (8) for 100 Lagrangian particles with initial conditions  $v = \sin(x)$  and  $z = \cos(x)$  (shown in blue). To aid visual comprehension, the particles of the same instance in time are connected by lines.

we integrate the equations for the particle velocity

$$\dot{v} = -\frac{v}{\tau_p} \quad (7)$$

(where the shorthand notation  $\dot{w}$  for an arbitrary function  $w(x, t)$  stands for  $\dot{w} = \partial_t w + v \partial_x w$ ) and the gradient  $z = \frac{\partial v}{\partial x}$

$$\dot{z} = -\frac{z}{\tau_p} - z^2, \quad (8)$$

(derived from Eq. (7) and similar to Eq. (6)) using 100 point-particles with the initial condition  $v = \sin(x)$  and  $z = \cos(x)$ , respectively. The motion of the particles is reduced to one dimension and (in contrast to Eq. (1)) a constant, zero-valued flow  $u = 0$  is prescribed. The results for three different values of  $\tau_p$  are displayed in Fig. 1, with the top- and bottom-row panels showing the time series of solutions to Eqs. (7) and (8), respectively. We observe that light particles (Figs. 1(a,d)) readily evolve in time towards  $v = 0$  and  $z = 0$ , respectively. The solution remains smooth and well-behaved at long integration times and both signals essentially vanish. In the intermediate case ( $\tau_p = 1$ ), the velocity gradient develops a sharp peak into the negative direction at  $x = \pi$ , yet remains bounded (Fig. 1(e)). For  $\tau_p = 3$ , Eq. (8) is unstable and  $z$  blows up to large negative values (Fig. 1(f)). A fold in  $x - v$  space develops, the hallmark of the caustic singularity. This is caused by the de-regularizing effect that inertia exerts on the particle dynamics. Clearly, the relaxation term on the right-hand side of Eq. (7) has a dampening effect on the system: it dictates how fast the solution converges to  $v = 0$ . At large  $\tau_p$ , the relaxation is slow and particles travel far enough to overtake one another in due time; a fold in phase space ensues. Caustic singularities can

only occur in Lagrangian flows. The Eulerian equation equivalent to Eq. (7),  $\frac{\partial u_p}{\partial t} + \frac{\partial(u_p^2/2)}{\partial x} = -\frac{u_p}{\tau_p}$ , on the other hand, corresponds to the inviscid Burgers equation with a source term on the right-hand side and thus can lead to shocks, if not sufficiently suppressed by the relaxation term (or by viscosity), but the weak solution always remains single-valued, whereas the particles in sling events effectively exhibit multivalued local velocities.

The results shown in Fig. 1 depict the solution to a distinctly simple particle-laden flow. In real turbulence and at high  $Re$ , particles are subjected to highly intermittent, 3D flows, which fluctuate on a range of time and length scales. Figure 1 illustrates, however, that even in the absence of a turbulent (or any, for that matter) signal, the dynamics of particles with large Stokes numbers are susceptible to the formation of caustics. In the following, we will briefly review recent advances in the field involving turbulent or statistical model flows.

Whether a caustic forms depends on the history of FVGs that the particles experience along their trajectories. Recently, Meibohm and co-authors<sup>18–20</sup> have investigated paths to caustic formation in the so-called *persistent limit*, in which particles have weak inertia ( $St \ll 1$ ) and see the flow as quasi-constant ( $Ku \gg 1$ ). The persistence of the flow is characterized by the Kubo number<sup>24</sup>  $Ku = \tau_\eta/\tau_a$ , where  $\tau_a = \eta/u_\eta$  is the advection timescale, i.e., the typical time it takes for a tracer to travel the distance  $\eta$ . It was demonstrated that ahead of participating in a sling event, particles reside in flow regions where the topology is dominated by strain overwhelming rotation (i.e.,  $Q < 0$ ) and by strain-rate self-amplification. The latter is characterized by large positive values of the third invariant of the FVG tensor,  $R = -\frac{1}{3}\text{tr}(\mathbb{A}^3)$ , which expresses the difference between enstrophy production and

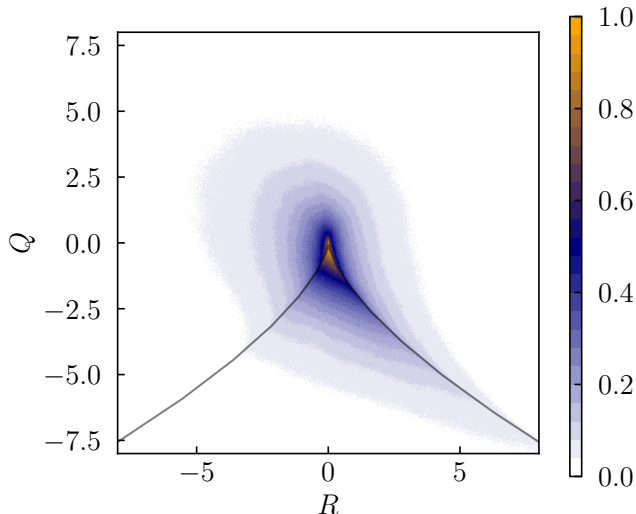


**FIG. 2:** Joint probability density of  $Q$  and  $R$  computed from a filtered DNS field, scaled with its maximum value. The vertical and horizontal axes are scaled with  $A_0$  and  $A_0^{-3/2}$ , respectively, where  $A_0$  is an arbitrary constant. The solid black line shows the Vieillefosse line. Note that the unfiltered flow fields qualitatively produce similar joint probability distributions (not shown).

dissipation production<sup>15</sup>. In contrast to the vast majority of particles, which expectedly sample  $\langle Q \rangle = 0$  and  $\langle R \rangle = 0$  along their paths (with  $\langle \dots \rangle$  representing Lagrangian time averages), particles that undergo caustics boast large excursions of the invariants ahead in time. Optimal fluctuations of  $Q$  and  $R$  that trigger caustics were derived of the form<sup>19</sup>  $Q(t) \sim -(A_{th}f(t))^2$  and  $R(t) \sim (A_{th}f(t))^3$ , where  $A_{th}$  is an  $St$ -dependent threshold and  $f(t)$  a strain correlation function, both determined empirically by fitting to simulation data.

Here, it is of significance to consider the plane spanned by  $Q$  and  $R$  in order to describe the dominant flow topology. Simulations and experiments of turbulence show that the joint probability density function (JPDF)  $p(Q, R)$  is skewed towards the fourth quadrant of the  $QR$ -plane<sup>15</sup> ( $Q < 0, R > 0$ ). There, the strain-rate tensor has two positive (stretching) and one negative (contracting) eigenvalue, and the flow topology is dominated by strain and strain production, i.e., strain-rate self-amplification<sup>14</sup>. The above-mentioned skewness of the JPDF is evident in Fig. 2, which is obtained from the sharp spectrally-filtered flow and also displays the so-called Vieillefosse line<sup>25</sup>  $(R/2)^2 + (Q/3)^3 = 0$ . Gradients concentrate around its positive branch ( $R > 0$ ), along which they self-amplify and create the most extreme values of  $\Lambda$ <sup>14,15</sup>. This exact flow topology that propagates along the positive Vieillefosse tail was shown by Meibohm *et al.*<sup>19</sup> to drive particles into sling events in statistical models of particle-laden turbulence. In real turbulence, on the other hand, caustics are driven by a range of FVGs that scatter broadly below the Vieille-

fosse line<sup>20</sup>, yet still qualitatively match the predictions from the statistical model. The results presented in these studies are limited to small Stokes numbers, specifically  $St \lesssim 0.3$ . At larger inertia, particles are more susceptible to instabilities, and non-optimal fluctuations of  $\Lambda$  become increasingly likely to cause  $Z$  to blow up. It remains unclear to what extent these findings generalize to turbulence at larger  $Re$ , smaller  $Ku$  and a wider range of  $St$ . Such regimes are relevant, e.g., for the collision of droplets in clouds and thus deserve attention.

Returning to the Eulerian approach introduced at the beginning of this section, Lee & Lee<sup>23</sup> solved Eq. (2) explicitly to perform DNS of particle density fields advected by 3D isotropic turbulence at a moderate Reynolds number of  $Re_\lambda = 14$ . The simulations were carried out until  $\xi$  diverged, which was then identified as the occurrence of a caustic. It was observed that sling events take place in thin layers of low vorticity and high strain, ‘packed’ in between turbulent vortices. The flow topologies of these regions coincided with the Vieillefosse line in the  $QR$ -plane.

These recent efforts to understand the sling dynamics of inertial particles underpin the adamant mystery posed by the formation of caustics in turbulent flows. The present work aims at further elucidating this phenomenon by providing observations of sling events of unprecedented detail on the basis of an extensive DNS campaign of particle-laden turbulence at large  $Re$ . We will verify the aptitude and limits of novel theories of caustics by identifying and studying sling events in fully-resolved turbulence with particles of Stokes numbers of up to  $St = 5$ . To the best of our knowledge, such results have up to now been limited to statistical flows or turbulence at  $Re \leq 200$  and  $St \leq 0.3$ . In addition, we will dissect the clustering mechanisms originating from the centrifuge and the path-history effect, and we will study the effect of filtering on the spatial distributions of the particle fields, which has important implications for modeling particle-laden turbulence in LES.

This paper is structured as follows. The numerical methods are described in Section II. The results are discussed in Section III, divided into three parts: First, we discuss instantaneous clustering and the relative importance of Maxey’s centrifuge and the history-path effect (Section III A). We then turn to the effect of the filter and show that scale-similar patterns are obtained (Section III B). Thirdly, we cover sling events and investigate the flow topologies that trigger caustics (Section III C). Finally, in Section IV, we summarize our findings.

## II. NUMERICAL SIMULATIONS

Direct numerical simulations of incompressible homogeneous isotropic turbulence laden with  $N_p = 5.4 \times 10^9$  mono-dispersed particles are performed. The turbulent flow fields are obtained from the public database of the Johns Hopkins University<sup>26</sup>. They are produced by a

**TABLE I:** Simulation parameters.

Case	$\kappa_c$	$\tau_\eta$	$\tau_p$	$Ku$	$St$	$St_{\text{eff}}$
DNS0.2	512	0.0424	0.0085	10.3	0.2	-
DNS1	512	0.0424	0.0424	10.3	1	-
DNS5	512	0.0424	0.2120	10.3	5	-
FDNS1	16	0.2165	0.0424	21.4	-	0.2
FDNS5	16	0.2165	0.2120	21.4	-	0.98

pseudo-spectral code with low-wavenumber forcing in a cubic domain of length  $L = 2\pi$  with periodic boundary conditions. The Fourier and physical space are discretized into  $2\kappa_{\text{max}} = 1024$  wavenumbers per dimension and  $N_g = 1024^3$  grid points, respectively. The Taylor-scale Reynolds number is  $Re_\lambda = 418$  and the Kolmogorov length scale is  $\eta = 0.0028$ . The simulation parameters are provided in Table I. The fields are given in non-dimensional units. Time is measured in terms of the DNS time, which is provided in intervals of  $\Delta t = 0.002$ . The method to calculate  $\tau_\eta$  after applying the filter and the definition of the filter-effective Stokes number  $St_{\text{eff}}$  are provided in Section III B.

We use an in-house parallel solver to integrate Eq. (1) in time for each particle using a simplified version of the scheme by Jenny *et al.*<sup>27</sup> The fluid velocity is evaluated at the particle positions by trilinear interpolation. Ireland *et al.*<sup>28</sup> report that in comparison to spectral interpolation, errors of up to 1% are incurred with linear interpolation schemes. We view this error as an upper bound to the present work, since a higher resolution is used. Interpolation errors are accepted; it was, however, verified that the method is conservative, i.e., that tracers do not cluster.

A sharp spectral filter with a cut-off wavenumber  $\kappa_c$  is used to truncate the turbulent energy spectrum such that the filtered velocity field is given by  $\bar{\mathbf{u}}(\mathbf{x}, t) = \sum_{\kappa: |\kappa| < \kappa_c} \hat{\mathbf{u}}(\kappa, t) e^{i\kappa \cdot \mathbf{x}}$ , where  $\hat{\mathbf{u}}(\kappa, t)$  is the Fourier mode of the flow velocity with wavenumber vector  $\kappa$ . The filter effectively removes all turbulent length scales smaller than  $\ell_c = \pi/\kappa_c$ . We note that the filtered velocity fields are distinctly different from synthetic flows or LES data, since the dynamics of all Fourier modes, i.e., the full turbulent energy spectrum, is resolved numerically, and the filter is applied a posteriori. The resulting fields can be considered *perfect*, representing model-free LES. However, we point out two differences compared to conventional LES: Firstly, we resolve the flow field on the original mesh with  $N_g = 1024^3$  grid points, even though  $N_g = 32^3$  nodes per dimension would suffice to resolve the truncated spectrum in physical space without significant loss of information. Essentially, this is spectral interpolation, which is avoided in LES in practice for obvious reasons. Secondly, the filtered flow field does not exhibit a dissipative range, since the filter sharply cuts the energy spectrum in the inertial range. Usually, SGS models, such as the Smagorinsky model, are used in LES. These models create an artificial dissipative range by in-

creasing the effective viscosity<sup>29</sup>.

Now, what is the role of the filter? The direct effect of the filter is that  $\mathbf{u}$  and  $A$  in Eqs. (1) to (4) and (6) are replaced by the filtered fields  $\bar{\mathbf{u}}$  and  $\bar{A}$ , respectively. These fluctuate on slower in time and on coarser length scales. While  $\tau_\eta$  is increased by a factor of 5, the advection timescale  $\tau_a$  roughly only doubles, meaning that the Kubo number increases from  $Ku^{(\text{DNS})} = 10.3$  to  $Ku^{(\text{FDNS})} = 21.4$ , shifting the system towards the persistent regime. In the context of particle-laden turbulence, it is important to emphasize that gradient self-amplification persists in the filtered field velocity<sup>14</sup>. This is verified by the plot in Fig. 2 based on our dataset of sharp-spectrally filtered DNS, where the characteristic sheared teardrop shape of the joint probability density of  $Q$  and  $R$  is recovered.

### III. RESULTS

#### A. Instantaneous clustering

The particles are initialized at uniformly distributed random positions with the local flow velocity. All cases start from identical initial conditions at the same instance in time. Since the particles do not have any memory when they are introduced into the flow, they cluster in the beginning solely due to the centrifuge mechanism. This initialization facilitates the treatment of the particle velocity as a continuum, a 'flow of particles'<sup>23</sup>, in the sense that Eqs. (2) to (4) are valid until a caustic occurs. Later on, the particle velocity field becomes locally multivalued, and the Eulerian equations must be abandoned in favor of Eq. (6).

Figure 3 shows the divergence of the particle velocity field alongside contours of the local instantaneous  $Q$  field at an early instance in time, at which particles have not yet acquired a significant amount of memory, and only very few particles paths have crossed. First, notice how the sharp spectral filter removes the smallest scales of the flow field and thereby smoothens the velocity gradients, as well as massively narrows the range that  $Q$  attains. The color map in Fig. 3(b) is clipped at  $Q = \pm 1000$ , preventing the contours from being washed out by extreme outliers. Nevertheless, intermittent small-scale regions of intense turbulence are observed, where  $Q$ , in reality, attains values of up to  $10^5$ . This reflects the nature of turbulence, as the smallest scales exhibit the most extreme vorticity and strain, produced by the non-linear self-amplification of the Navier-Stokes equation. Second, notice the excellent visual agreement between the contours of the divergence patterns (Figs. 3(a,c)) and  $Q$  (Figs. 3(b,d)). 'Particle sinks' with positive values of  $\xi$  emerge in regions where  $Q$  is large and positive, i.e., where particles are ejected out of vortices. Particles accumulate, on the other hand, where  $\xi$  is negative, leading to an increase of the particle density via Eq. (3). These regions coincide with large negative values of  $Q$ , i.e., where

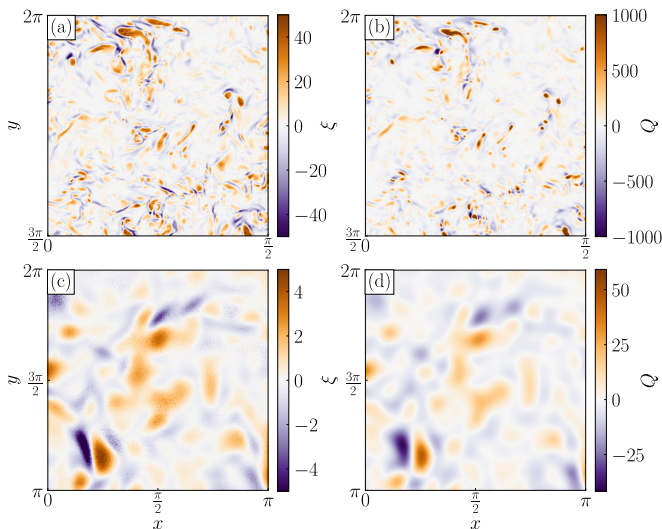


**FIG. 3:** Instantaneous clustering at short integration times. Grid-projected particle velocity divergence fields of the (a) DNS5 and (b) FDNS5 cases at time  $t = 0.04$  and  $t = 0.08$ , respectively. In panels (b) and (d), contours of the local instantaneous  $Q$  fields are shown. The contours of panel (b) are clipped to the range  $-1000 \leq Q \leq 1000$ , in order to hide the rare extreme excursion of the unfiltered field in the color map, whereas the  $\xi$ -fields in the panels (a) and (c) are clipped to  $-50 \leq \xi \leq 50$  and  $-5 \leq \xi \leq 5$ , respectively.

strain overwhelms vorticity. In other words, the instantaneous flow field explains the spatial distribution of the particles well at this early stage, and Maxey’s centrifuge gives qualitatively accurate predictions of clustering.

Figure 4 visualizes the particles in thin slices of thickness  $s = \eta$  after long integration time with the contours of local instantaneous  $Q$  in the background. The particles shown have reached steady state, both in terms of the density variance  $\langle (n - \langle n \rangle)^2 \rangle$  and its anti-correlation to  $Q$ . The sharp spectral filter was applied to the flow in the background of the DNS5 case displayed in Fig. 4(c) in order to remove turbulent eddies with timescales  $\tau < \tau_p$  from the flow; in the simulation, however, the unfiltered flow was used.

While Fig. 3 showed how the granularity of the flow is imprinted on the particle fields after initializing the simulations, Fig. 4 illustrates that the coarseness of the particle distributions persists even after long integration times. We remark that additional simulations were performed in which the particles were initialized with randomly sampled isotropic velocities. The imposition of the particles’ granularity by the flow field was also observed in that case (not shown). In fact, the patterns that emerged after long integration times showed little to no differences to those observed in Fig. 4. The persistence of the particle field granularity implies that SGS velocity fluctuations are needed in LES to recover qualitatively accurate spatial distributions of inertial particles.

Clearly, particle clustering is observed in all cases. In the DNS1 case with  $St = 1$ , which is known to ex-

hibit the most intense preferential concentration, clusters are thin, curved structures that are elongated along the local flow topology. Indeed, Eq. (5) seems to predict the spatial distribution of the particles qualitatively well in this case, even after long integration times. As expected<sup>17</sup>, these patterns match the typical range of preferential concentration,  $\ell \sim 10\eta$ , with void sizes spanning into the inertial range of turbulence. A prominent large gap in the particle fields (located in the region  $(\frac{\pi}{2} \leq x \leq \pi, 0 \leq y \leq \frac{\pi}{2})$ ) is seen in all unfiltered cases, coinciding with the largest connected region of increased  $Q$  of the coarse field (Fig. 4(c)). Similarly to the DNS1 case, the DNS0.2 particles ( $St = 0.2$ ) avoid high- $Q$  and populate low- $Q$  regions, respectively. Particle voids are, however, more exclusive to the most intense vortices. In-between clusters, the particles are distributed more uniformly, and small-scale filamentary patterns are observed. The path-history effect produces fractal clusters with a decrease in the fractal dimension as the Stokes number is increased from  $St = 0.2$  to  $St = 1$ . In the DNS5 case ( $St = 5$ ), the particles are too heavy to resonate with the smallest scales of the flow field, which act to randomize the particle fields and impose their granularity. Once the fine scales are removed, qualitative agreement between clusters (voids) and low (high)  $Q$  regions is observed, as seen in Fig. 4(c). Clustering agrees best with the most significant coarse-grained flow contours that match the particle timescale,  $\tau_p$ . Note that the background in Fig. 4(c) was obtained by filtering the flow field explicitly to match  $\tau_p$ , i.e., so that only turbulent structures of timescale  $\tau \leq \tau_p$  are removed. This provides evidence for the self-similarity of particle clusters, previously reported by Goto and Vassilicos<sup>30</sup>. The authors’ reasoning is based on the premise that turbulence consists of a hierarchy of self-similar eddies across different length scales, each resonating with particles of a specific  $\tau_p$ .

In the filtered cases (Figs. 4(d,e)), instantaneous preferential sampling does not explain clustering well. Both cases exhibit significantly elevated particle number density in low and high  $Q$  regions. Moreover, the spatial distributions reveal intricate structures with filamentary patterns. The particle density fields are highly intermittent, with sharp edges separating clusters from voids. The sharp edges are seen because the number of particles remains unchanged between the unfiltered and filtered cases, yet the resolution is higher relative to the smallest scales. Filaments are most conspicuous in the FDNS1 case, where particles fill the domain more uniformly; however, they are also seen in FDNS5, where caustics contribute to the formation of highly irregular patterns. Small-scale filamentary clusters that do not coincide with the local patterns of strain or vorticity have been observed before (e.g. in Fig. 1(b) in Ref. 7), yet the strong misalignment of particle density and  $Q$  as well as the large length scale at which filaments are seen are surprising. A possible explanation for the discrepancy between the effectiveness of the centrifuge mechanism to



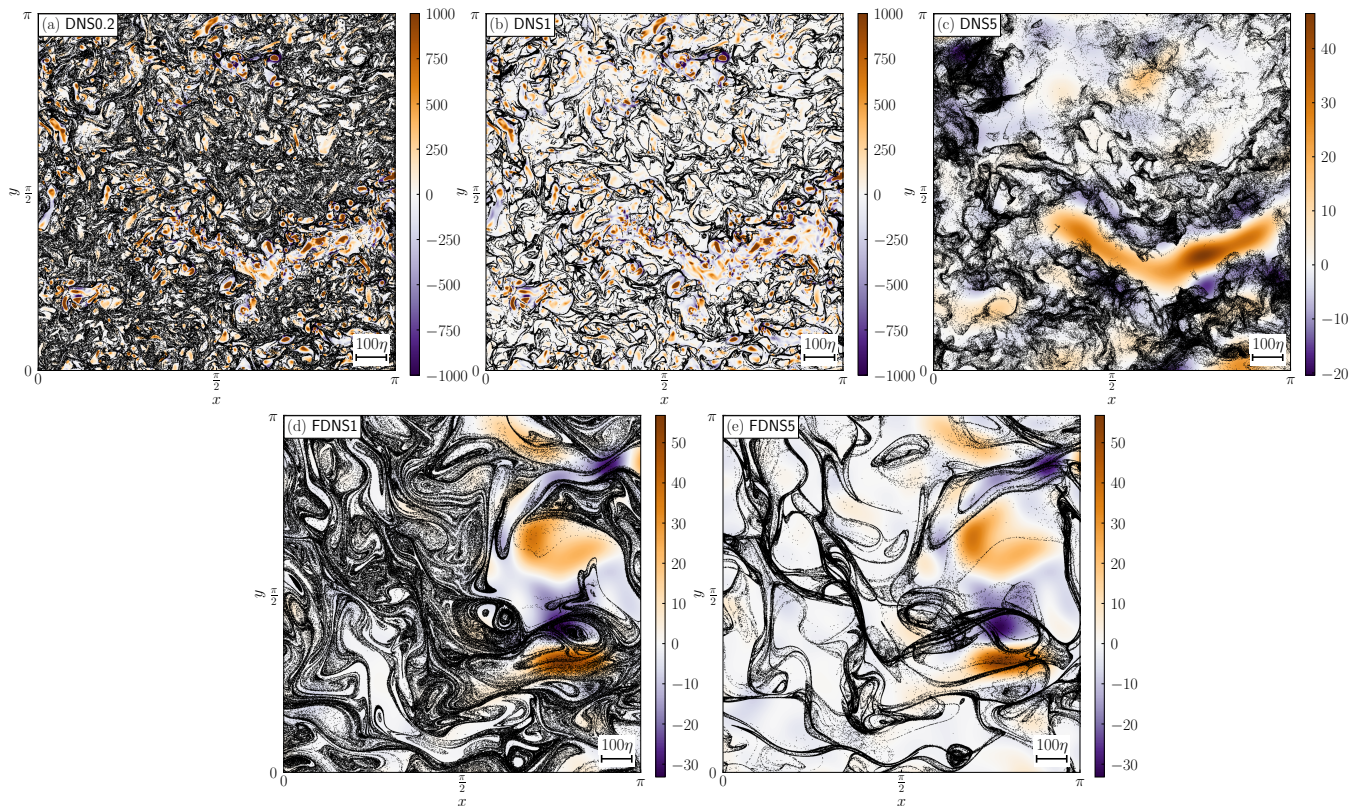


**FIG. 4:** Spatial distribution of particles at steady state, with contours of  $Q$  in the background. The particles inside a slice of thickness  $s = \eta$  are represented by black dots. Only a quarter of the domain is shown. As in Fig. 3, the range of  $Q$  is clipped in panels (a) and (b). Note that the background of panel (c) is obtained from the filtered flow field, even though the particles are suspended in the full-spectrum unfiltered flow.

explain clustering in the unfiltered and filtered cases is that the filter removes the regions of the most extreme vorticity and strain, inherent to the dissipative scale of turbulence. We are not convinced by this explanation, however, as, in the smallest scales, the particle fields of the unfiltered cases reveal similar patterns that cannot be attributed to the instantaneous flow field. This is shown in the following section.

## B. Scale similarity

Filtering out small-scale turbulent motions leads to an increase in the characteristic flow timescale. For the filtered fields, this timescale is calculated as<sup>7</sup>

$$\bar{\tau}_\eta = \langle \text{tr}(\bar{A}\bar{A}^T) \rangle^{-1/2}. \quad (9)$$

(Note that, for the sake of simplicity, the symbol  $\tau_\eta$  was used without an overbar in Table I for all cases.) We then define the filter-effective Stokes number as  $St_{\text{eff}} = \tau_p / \bar{\tau}_\eta$ . With the Stokes numbers adjusted to the timescale of the filtered flow, we expect to observe similar fractal properties (i.e., matching correlation dimensions) and spatial patterns between the DNS0.2 and FDNS1, as well as between the DNS1 and FDNS5 cases, respectively.

Now, at what length scale should the spatial patterns of the unfiltered and filtered cases be compared? Here, it is important to recall that the filtered fields are obtained by sharply truncating the Fourier spectrum at a wavenumber in the inertial range,  $\kappa_c = 16$ . The filtered fields therefore do not exhibit a dissipative range. Even though the subscript  $\eta$  is used for the filtered flow timescale (Eq. (9)), it may not be thought of as the ‘Kolmogorov’ timescale. In fact, the notion of the Kolmogorov range of turbulence is not applicable to the filtered fields. While Eq. (9) is a valid expression for the characteristic timescale, the identification of the reference *length* scale is more complicated. Ray and Collins<sup>13</sup> use the filtered energy spectrum to compute the dissipation as  $\bar{\epsilon} = 2\nu \int_0^{\kappa_c} \kappa^2 E(\kappa) d\kappa$ , where  $E(\kappa)$  is the turbulent kinetic energy associated with the Fourier mode  $|\kappa| = \kappa$ . The reference length scale of the filtered fields was then calculated as  $\bar{\eta} = (\nu^3 / \bar{\epsilon})^{1/4}$ . This quantity is, however, elusive in our setup, as nearly all of the dissipation of turbulent kinetic energy occurs in the dissipation range, i.e., at the largest wavenumbers.

Here, we introduce an ad hoc method to estimate the length at which the unfiltered and filtered cases should be compared: We compute the ratio between the largest wavenumbers arising in the inertial range of

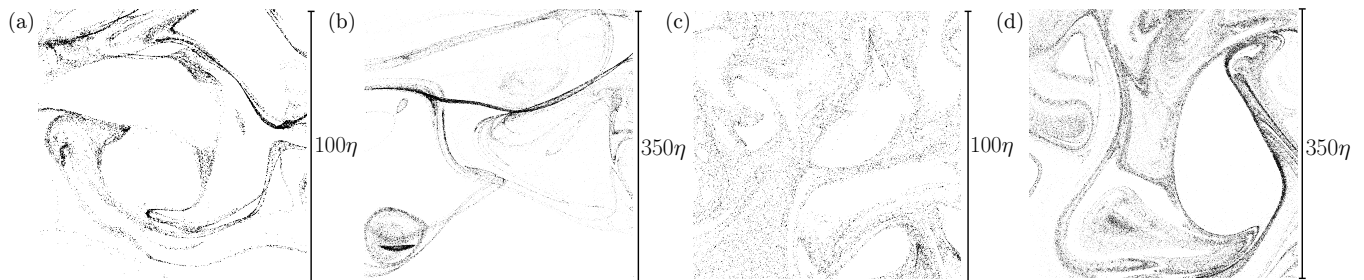


**FIG. 5:** Scale-similarity of the particle fields from the unfiltered and filtered at matching (effective) Stokes numbers. Particles in a slice of thickness  $s = \eta$  are shown as black dots. (a) DNS1 with  $St = 1$ , (b) FDNS5 with  $St_{\text{eff}} = 0.98$ , (c) DNS0.2 with  $St = 0.2$ , and (d) FDNS1 with  $St_{\text{eff}} = 0.2$ .

**TABLE II:** Correlation dimensions.

Case	$St$	$St_{\text{eff}}$	$d_2$
DNS0.2	0.20	-	2.64
FDNS1	-	0.20	2.73
DNS1	1.00	-	2.33
FDNS5	-	0.98	2.41

the turbulent flow in the filtered and the unfiltered flow fields, that is the filter cut-off and the end of the inertial range,  $\kappa_{DI}/\kappa_c \approx 3.5$ . The 1-to-3.5 scaling is employed in Fig. 5, which shows slices of particles of the cases DNS1, FDNS5, DNS0.2 and FDNS1. The length scales of clusters and voids are comparable. We are again confronted with filamentary patterns observed earlier in the spatial distributions shown in Fig. 4. In addition, there is a noticeable decrease in the extent to which particles fill the domain as the (effective) Stokes number increases, suggesting a reduction in fractal dimension.

Scale similarity between the DNS1 and FDNS5 as well as between the DNS0.2 and FDNS1 cases is visually evident, i.e., similar patterns are observed when magnified to the appropriate level. The DNS1 clusters are revealed to have internal structure which was previously (Fig. 4(b)) not visible. These patterns are indicative of multiplicative amplification, which, in simulations of statistical models<sup>7</sup>, is observed at length scales even smaller than  $\eta$ . Numerical studies comparable to the present work usually do not resolve such structures and thus obtain particle fields that can be explained well at sufficiently large scales based on the instantaneous flow fields, not unlike panels (a) or (b) in Fig. 4. Some examples are Fig. 2(a) in Ref. 17, Fig. 2 in Ref. 11, or Fig. 5 in Ref. 31. Based on the visual evidence provided by 5(a), however, it must be expected that small-scale filaments are present throughout, yet usually not visible due to the level of magnification or unresolved due to an insufficient number of particles. These filaments are the result of multiplicative amplification, and their arrangement does not align well with the instantaneous flow field.

In line with Ref. 16, the fractal dimension of the particle distributions decreases with increasing Stokes num-

ber. Measurements of the correlation dimensions are provided in Table II. The values were obtained by performing polynomial fits over the radii  $r/\eta \in \{0.5, 1, 1.5, 2\}$  and averaging over ensembles of 75 randomly selected test particles for each case. The  $St$ -dependence of the correlation dimension matches the values from the literature, recently collected by Bec *et al.*<sup>17</sup> The effective Stokes number therefore approximately predicts the fractal quality of the particle clusters. We also find that unfiltered and filtered cases with comparable (effective) Stokes numbers yield similar correlation dimensions, confirming spatial scale-similarity quantitatively.

### C. Sling events

We now turn to the discussion of sling events, which occur throughout our simulations. In the following, we provide detailed observations of these events and test the applicability of new theories for their prediction. Patterns of caustics are observed in all cases, as seen in Fig. 6, which shows particles scattering in the computational domain after short integration times. We emphasize that modeling the particle motion using an Eulerian continuum formalism (Eq. (2)) is clearly not suitable under these circumstances, as significant numbers of particles undergo caustics and therefore attain multivalued velocities at the same location in space and time (see one-dimensional model presented in Section I). In the filtered cases, caustics are conspicuous thanks to their warped manifold structure at comparatively large length scales, populated by large ensembles of particles. Figure 6(d) visualizes the peculiar patterns that are associated with sling events at large Stokes number. Heavy particles exhibit high relative velocities and form ‘pockets’<sup>32</sup> (triggering collisions in reality), whereas lighter particles have lower memory capacity and adjust to the flow easily, meaning that lower relative velocities are attained during caustics. This explains the absence of pockets in the FDNS1 case, where caustics appear as lines (sheets in 3D). The pockets in the FDNS5 case are framed by sharp lines of high particle number density, which will be shown to exhibit maximal relative velocities (Fig. 7). A



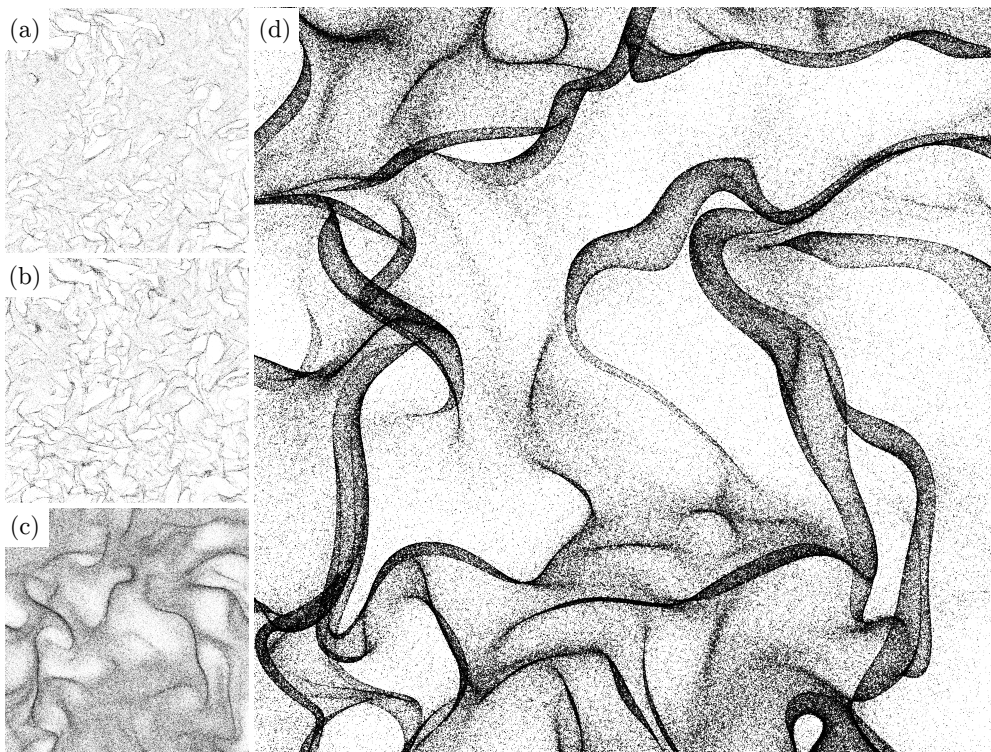


**FIG. 6:** Caustic patterns in unfiltered ((a) DNS1, (b) DNS5) and filtered ((c) FDNS1, (d) FDNS5) turbulence at times (a,b)  $t = 0.012 \approx 3.8\tau_\eta$  and (c,d)  $t = 0.8 \approx 2.8\tau_\eta$ . The particles in a slice of thickness  $s = \eta$  are depicted as black dots. Panels (a,b) show an eighth of the domain, whereas (c,d) show a quarter.

3D visualization of the pocket character of sling events in the FDNS5 case is provided as supplementary material in Fig. 12(b).

Now, how do we classify the particles that participate in caustics? Meibohm *et al.*<sup>18–20</sup> integrate Eq. (6) alongside Eq. (1) for each particle and identify sling particles as those that reach  $\text{tr}(\mathbb{Z})$  below a critical value. Similarly, Lee & Lee<sup>23</sup> use an Eulerian model for the particle motion and identify caustics as blowups of Eq. (4). Both methods are meaningful in that they provide the exact instance in time at which the caustic occurs, yet they are computationally inconvenient. In this work, a simpler, computationally cheaper method is used to condition the particles. Our approach exploits the key characteristic of the caustic: multivalued particle velocities, i.e., close-by particle pairs  $(l, k)$  having large relative velocities  $d\mathbf{v}_{lk} = |\mathbf{v}_l - \mathbf{v}_k|$ . For each particle, we compute  $D = \langle d\mathbf{v} \rangle_{3nn}$ , where  $\langle \cdot \rangle_{3nn}$  is the ensemble average over the 3 nearest neighbors, which are only accounted for if all three particles are not further away than  $\eta$ . Particles that do not have at least three neighboring particles inside the sphere of radius  $r = \eta$  are exempted. We then pick a suitable instance in time,  $t_c$ , and identify particles with  $D$  exceeding a certain threshold,  $D_c$ .

Our method is computationally convenient and can be applied to any numerical simulation that uses particle tracking, without requiring the integration of additional equations. No extra fields need to be tracked, and the

FVG tensor only needs to be computed at time  $t_c$ , eliminating the need to calculate and store both  $\mathbb{A}$  and  $\mathbb{Z}$  for each particle at every time step. However, we acknowledge that, unlike methods that explicitly track blow-ups in Eq. (6), our method is not able to capture the *exact* instance in time when the caustic occurs. When computing the instantaneous relative velocities, there is some uncertainty associated in whether a particle has just reached a large value of  $D$ , i.e., if the caustic has *just* occurred, or whether the particle is currently in the onset of a caustic and the main jump in  $D$  is yet to take place. A preliminary study, however, indicated that particles tend to undergo swift, steep increases in  $D$ , rather than smooth ascents over longer periods of time. Uncertainty in the peaks of  $D$  is especially limited in the unfiltered cases, where the spikes take place over the course of only a few time steps.

As described in Section II, Eq. (1) is solved in three dimensions for a large ensemble of particles that lag the turbulent carrier gas flow. We find that caustics form readily, and as early as after  $t \approx 2\tau_\eta$ . To provide an example, we visualize the identification of a sling event in the FDNS5 case in Fig. 7. The large panels depict the particles scattering in a thin slice at three instances in time, colored based on the value of  $D$ . A slender area of increased relative velocity is easily identified. The sling region, initially a thin line in Fig. 7 (a) (implying a sheet in 3D), attracts particles and grows in width to an elon-

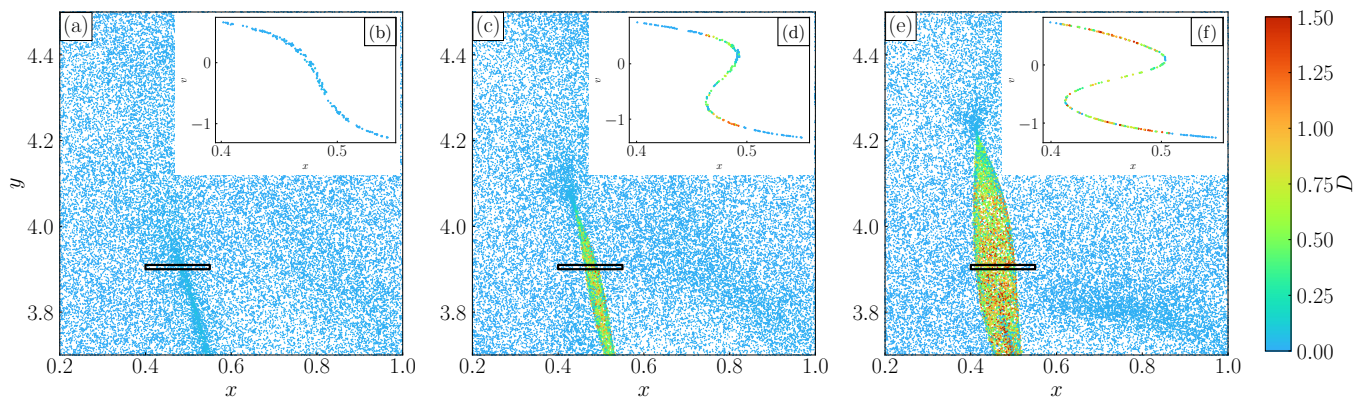


**FIG. 7:** Identification of a caustic in a sling event, obtained in the FDNS5 case after (a,b)  $t = 0.14$ , (c,d)  $t = 0.2$  and (e,f)  $t = 0.28$ . Panels (a,c,e) show the particles scatter in a slice of thickness  $s = \eta$ , colored in the ensemble-averaged relative velocity  $D$ , while the insets (b,d,f) depict the  $v$ - $x$  phase-space of the particles inside the indicated region.

gated cusp. This indicates that, independent of Stokes number, sling events occur on thin sheets, and that pockets (as seen in Fig. 6(d)) develop later in time at large enough  $St$ . Particles with opposing velocities approach each other from the negative and positive  $x$ -directions and cluster in the region around  $x \approx 0.5$ . Here, the particles are focused into a narrow region and the particle number density increases locally by a factor of around 2.5 (not shown). The transition from a smooth, unambiguous to a multivalued particle velocity field is evident from the insets in Fig. 7, showing the phase space composed of the first velocity and position components of the particles inside the small volume spanning across the caustic and marked by the black rectangle. The signal folds over itself, not unlike the one-dimensional model problem seen in Fig. 1. The insets also reveal that the largest relative velocities exist towards the edge of the caustic manifold, where 'new', freshly supplied particles are introduced into the sling area. In this region, particle collisions would occur most violently, as particles undergo a sharp increase in relative velocity.

In Fig. 7, we have illustrated the identification of a sling event by conditioning particles on the nearest-neighbor averaged relative velocity,  $D$ , and demonstrated how phase-space folds occur in these regions. To build on this, we now depict the flow conditions experienced by particles leading up to the occurrence of a caustic. For the first time to the best of our knowledge, we present 3D renderings of a sling event in Fig. 8. The visualizations are derived from the FDNS1 case, with individual particles represented as points at three consecutive time instances, colored in the locally experienced value of  $R$ . As described above, the ensemble of sling particles is selected at time  $t_c = 0.6$  using the condition  $D(t = t_c) > D_C$ . The time instance  $t = t_c$  is shown in panel (c), clearly revealing that the sling event occurs on a thin, warped sheet in 3D space. The selected ensemble is then tracked backward in time, and the local flow conditions are interpolated to the particle positions to obtain Figs. 8(a,b)

at times  $t = 0.2$  and  $t = 0.4$ , respectively. An additional 3D visualization of the backtracking of sling particle trajectories is provided in the appendix (Fig. 12).

Long before the caustic occurs, the 'epicenter' of the sling event can be identified in Fig. 8(a). This area features elevated  $R$ , but particles have not clustered or collided yet. In the following, the particles inside a dumbbell-like volume approach the epicenter, in which, under the compressive straining of the flow, particles converge on a thin, compact sheet. At time  $t = t_c - 0.2$  (Fig. 8(b)), the 'sling sheet' commences to take shape, and it is likely that particles in this region already experience elevated relative velocities. Eventually, all particles coalesce into a smooth manifold whose thickness is of the order of the particle diameter (Fig. 8(c)). The fact that we see the sling event taking place on thin sheets is due to the flow topology in the fourth quadrant of the  $QR$ -plane, where straining acts compressive in one and expanding in the other two directions. Owing to the low effective Stokes number  $St_{\text{eff}} = 0.2$ , however, the particles collide with comparatively low relative velocities, and  $D$  decreases rapidly after  $t = t_c$ , as the particles relax to the local flow field and coalesce back into a smooth flow of particles. In the FDNS5 case, on the other hand, particles collide at much higher relative velocities and the sheet structure is not retained later in time (see also Fig. 12(b)). The reason is that the heavier particles cannot adapt to changes of the flow velocity swiftly. This results in higher relative velocities at the time of the sling event and longer times during which they are retained. The crossing of particle paths is responsible for the development of pockets.

While the 3D renderings of Fig. 8 only depicts particles that actually participate in the sling event, Fig. 9 provides a 2D view of particles for which no particular selection was applied. The figure shows particles of the FDNS5 case at time  $t = t_c + 0.2$  (same time instance as in Figs. 7(c,d)) as arrows pointing in the direction of the  $x, y$ -velocities. The contours  $Q$  are shown in the back-



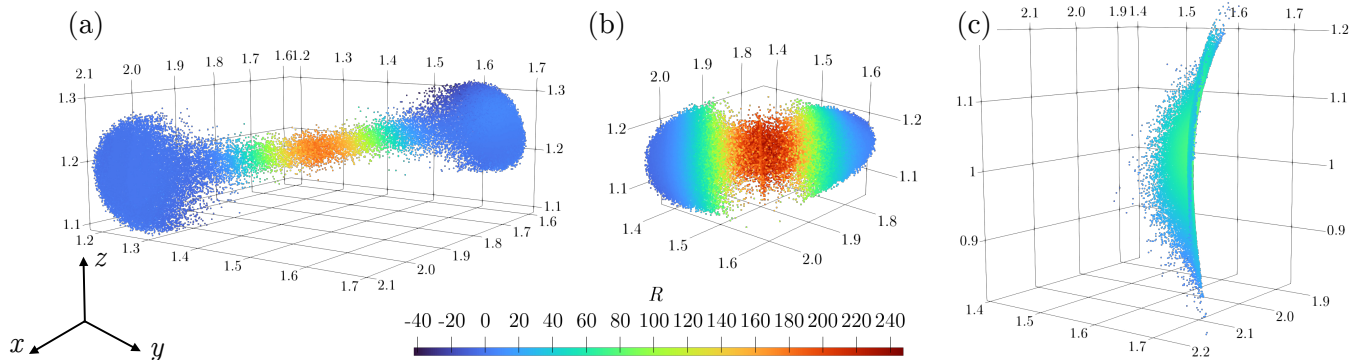


**FIG. 8:** 3D renderings of a sling event from the FDNS1 case at times (a)  $t = t_c - 0.4$ , (b)  $t = t_c - 0.2$  and (c)  $t = t_c$ , colored in the locally experienced  $R$ .

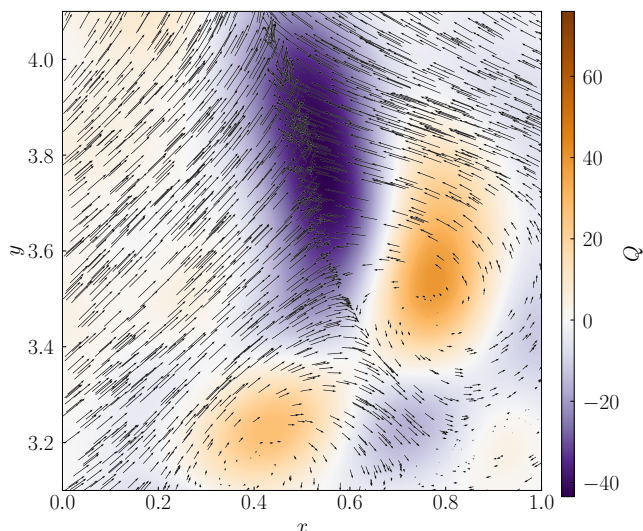


**FIG. 9:** Onset of a sling event in the FDNS5 case at  $t = t_c = 0.2$ . The  $x$ - $y$  velocities of the particles in a slice of thickness  $s = 0.03\eta$  are depicted as arrows, whereas the contours of local  $Q$  are shown in the background.

ground and delineate two vortices, separated by a region of intense strain around  $x = 0.5$ . The flow directions of the particles visualize the sling event that takes place in the  $Q < 0$  region. Here, the particle velocities are multivalued due to the occurrence of the caustic, as observed in Fig. 7(d).

Figure 9 also depicts the  $Q$ -conditions that particles experience before participating in the sling event. The flow directions indicate that particles are centrifuged out of the vortical structures and then engage in sling dynamics. However, not all particles that escape the  $Q > 0$  regions will participate in the sling event. For examples, those that are transported in the negative  $y$ -direction do not attain multivalued velocities. This indicates that, upon being ejected out of the vortices, a prolonged residence in flow topologies of compressive strain is required

for a particle to participate in a sling event. This is the case for flow topologies that progress along positive branch of the Villefosse tail. Figure 9 is consistent with the finding by Lee & Lee<sup>23</sup> that caustics occur in sheets 'packed' in between vortex layers. Particles are ejected out of vortices from opposite sides and, under compression strain from the turbulent motion, collide in between, where the curl is low and strain dominates. This insight is not contradictory to the traditional picture of preferential concentration, however the centrifuge mechanism appears to merely act as preconditioner for caustics.

The visual observations from Figs. 8 and 9 point to the fact that particles undergoing caustics experience intense turbulent motion in which they sample FVGs heterogeneously. As a matter of fact, throughout our simulations, sling particles move through flow topologies of large negative  $Q$  and large positive  $R$ . This statistical bias away from  $\langle Q \rangle = \langle R \rangle = 0$  is clearly evident in Fig. 10, which visualizes the most likely paths that sling particles take in terms of the FVG tensor invariants. The figure was produced as follows: For each case, we fix the threshold  $D_c$  and identify an ensemble of sling particles at time  $t = t_c$  (marked by the vertical black lines in Fig. 10) using the condition  $D(t = t_c) > D_c$ . These particles are then tracked backward in time (see Fig. 12 for a supplementary visualization) and each point along the particle trajectories, the probability densities  $p(Q)$  and  $p(R)$  of the ensembles are computed. The threshold  $D_c$  was adjusted slightly between the different cases in order to ensure similar numbers of tracked particles, which is necessary since the particles collide at vastly different relative velocities, depending on the Stokes number. It was, however, ensured that the choice of  $D_c$  in the ranges considered has only minor influences on the trajectory densities shown in Fig. 10. We found that the higher we chose  $D_c$ , the more extreme excursions of  $Q$  and  $R$  particles experience, however the curves of the fluctuations remain identical in shape. We note that alternative methods that track blowups of Eq. (6)<sup>19,20</sup> or Eq. (4)<sup>23</sup> are not exempted from the choice of an ad-hoc threshold, and we expect

that the distributions over ensembles of sling particles of  $\text{tr}(\mathbb{Z})$ , computed by explicitly integrating Eq. (6), also varies considerably with the Stokes number.

First, note how the scales of  $Q$  and  $R$  along the trajectories differ significantly between the filtered and unfiltered cases. In unfiltered turbulence, violent short-lived excursions of  $\mathbb{A}$  are obtained, with isolated particles escaping to values of  $R = 10^6$  and  $Q = -10^4$  (hidden by the axes limits of Fig. 10). This is a consequence of the well-known nature of turbulent flows to produce the most extreme strain and vorticity intermittently in the dissipative range<sup>15</sup>, offering a possible explanation to why sling events are observed at higher frequency in the unfiltered cases. In clouds, it is believed<sup>33</sup> that high levels of intermittency (owing to large Reynolds numbers of up to  $Re_\lambda \sim 10^4$ ) are responsible for the sling dynamics, enhancing collisions and coalescence of droplets, which initiates rainfall. The filter decreases the probability of rare extreme events in the flow field. This reduces the likelihood that particles will encounter the persistent intense flow topologies necessary to trigger caustics.

Qualitatively, the shapes of the excursions away from  $Q = 0$  and  $R = 0$  exhibit only minimal differences between DNS0.2 and DNS1. In fact, both Figs. 10(a,b) enjoy significant visual agreement to Fig. 3 in Ref. 19, which was produced by tracking particles with a Gaussian model at  $St = 0.3$  and  $Ku = 22$ ; as well as to the optimal fluctuations derived in the persistent limit. This indicates that qualitative agreement reaches far into the non-persistent (recall that in the DNS1 case,  $St = 1$  and  $Ku = 10.3$ ) regime and to fully-resolved, high-Reynolds number turbulence. Comparison of Figs. 10(a) to (b) and Figs. 10(d) to (e), respectively, verify that the conditions in terms of the fluctuation of  $\mathbb{A}$  required to initiate a caustic relax with increasing Stokes number. In other words, heavier particles are driven into sling events more easily, consistent with our observation of the regularizing effect of the  $1/\tau_p$  term on the right-hand sides of Eqs. (7) and (8). The most probable fluctuations, however, remain similar in shape.

Ahead of and after the sling event, particle trajectories are biased by preferential sampling. This is indicated by the fact that while  $Q$  deviates from zero significantly (relative to the peak of the fluctuation) outside the fluctuation, elevated  $R$  is only seen in a narrow timespan before and shortly after the sling event. In this regard, the notion of preferential sampling as a preconditioning mechanism for caustics is convincing: The centrifuge causes particles to preferentially sample  $Q < 0$  regions. If, by chance, these regions coincide with  $R > 0$ , particles are driven into a sling event by propagating along the positive branch of the Vieillefosse line (Fig. 11). This is manifested by a fluctuation to positive  $R$  and negative  $Q$ . The  $Q$ -preconditioning is less intense at  $St = 0.2$ , which makes caustics rarer and requiring more extreme fluctuations of the FVG.

As mentioned earlier, our method cannot predict the *exact* point in time at which the blow up of  $\text{tr}(\mathbb{Z})$  occurs.

The vertical lines in Fig. 10 merely depict the point in time at which  $D$  is measured compared to the threshold  $D_c$ . Our method's uncertainty in matching the point in time at which the caustic occurs is reflected by the artifacts of particles undergoing secondary fluctuations visible in Fig. 10(d). These indicate that the sling event takes place before or after we record the relative velocities. The vast majority of particles, however, are selected at a reasonable time. The variance is lower in the unfiltered cases, as the fluid timescales are much shorter, whereby particles peak in relative velocity during a very brief period of time.

Conspicuously, the sling particles of the DNS5 case (Fig. 10(c)) encounter extreme gradients from early on. Almost all of them are initially located in regions of negative  $Q$ , with the deviation from  $R = 0$  lagging slightly but still increasing early in the process. In other words, this leads one to suspect that for a particle with  $St = 5$ , the only prerequisite for participating in a sling event is to be initialized in a region of large negative  $Q$  at the start of the simulation and then being ejected into a  $R \gg 0$  region shortly thereafter. In truth, however, a history of FVGs that propagates along the Vieillefosse line is required for a caustic to occur, irrespective of the Stokes number, as shown in Fig. 11. At  $St = 5$ , sling events take place on shorter timescales, yet are caused by turbulent flow topologies in a manner very similar to the lower  $St$  cases. We do, however, expect that sling events can only occur below a certain Stokes number, as particles become too heavy to respond to the flow at some point and instead move ballistically.

In Fig. 11, it is observed that the gradients do not scatter on, but slightly below the positive branch of the Vieillefosse tail. An explanation for this circumstance was provided by Meibohm *et al.*<sup>20</sup>. In turbulence, strain and vorticity of the smallest scales is coupled in a way such that the vorticity reduces the dissipation production, shifting  $R$  to the left. Note that qualitatively similar joint probability densities were obtained in the filtered cases, which are not shown in Fig. 11 as they do not provide any further insight.

#### IV. CONCLUSIONS

In this work, we have obtained results from extensive direct numerical simulations of high-Reynolds number turbulence laden with large ensembles of one-way coupled inertial point-particles. The simulations were performed before and after applying a sharp spectral filter to the flow fields. The particles initially cluster where the local instantaneous strain dominates the vorticity, imposing granularity on the spatial distribution that is retained later on. The filter is shown to not only modify this granularity, but to also have strong effects on clustering by altering the relative importance of the mechanisms at play. While in the unfiltered cases, Maxey's centrifuge is found to be qualitatively accurate, the filtered fields

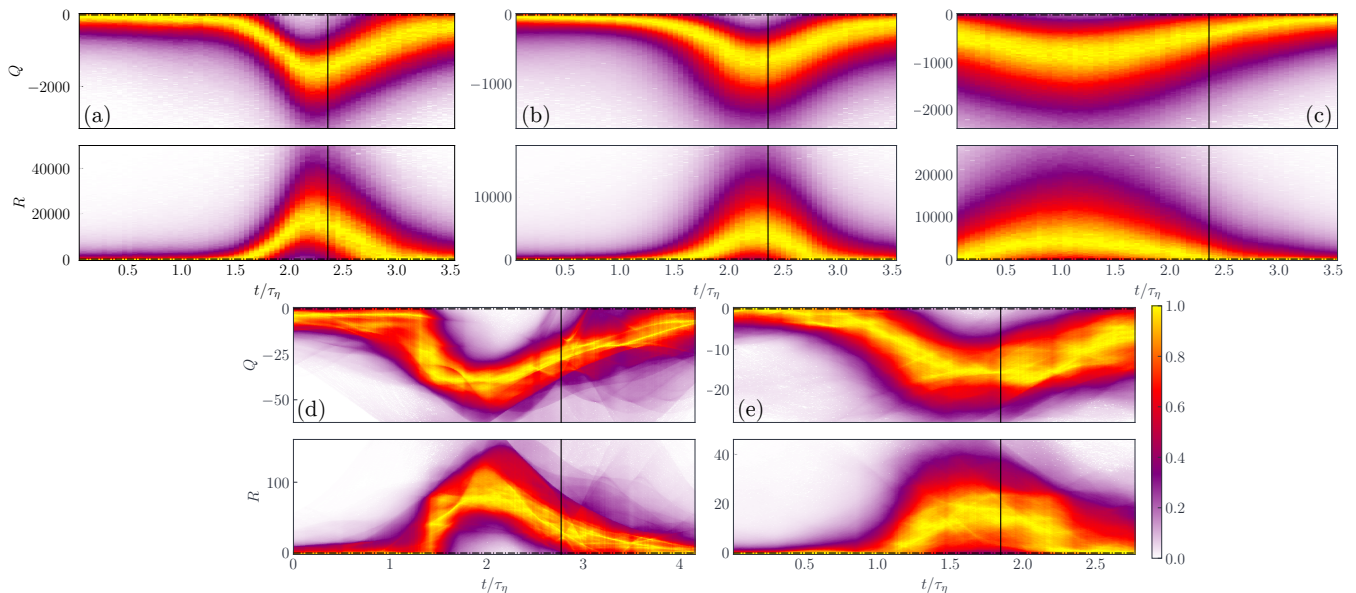


**FIG. 10:** Time evolution of the densities of  $Q$  and  $R$  along sling particle trajectories for the cases (a) DNS0.2, (b) DNS1, (c) DNS5, (d) FDNS1, (e) FDNS5. At each time step, the trajectory density is scaled by the maximum value. The black vertical lines depict the time  $t_c$  at which the sling particles are selected.

exhibit small-scale heterogeneity that can only be explained by the path-history effect. An effective Stokes number is used to compare unfiltered to filtered cases, and it is shown that scale-similarity holds at similar (effective) Stokes numbers; qualitatively in terms of the visual observations of the particle fields, and quantitatively in terms of the fractal correlation dimension. We then identified caustics by thresholding the relative velocities of close-by particle pairs and provided one-, two-, and three-dimensional visualizations of sling events, which occur as a result of rare, intense events of the turbulent flow field. Sling events were shown to take place in thin sheets, under compressive strain and biased by preferential sampling of the flow topology of the fourth quadrant in the  $QR$ -plane. A characteristic optimal fluctuation in terms of  $Q$  and  $R$  was observed to drive particles into sling events, suggesting that the recent results from Meibohm *et al.*<sup>19,20</sup> may extend to high-Reynolds turbulence beyond the persistent regime. The separation of mechanisms indicates that preferential sampling is most intense around  $St = 1$ , whereas clustering by caustics peaks somewhere above  $St > 1$ . These findings are, however, inconclusive and shall be investigated in more detail in future work.

Regarding Euler-Lagrange large eddy simulations of particle-laden turbulence, our results indicate that without models accounting for the sub-grid scales seen by the particles, significant errors are incurred. The absence of small-scale turbulence strongly alters the spatial distributions of the particles and the rate at which caustics occur. Clearly, sub-grid caustics cannot be resolved in LES. In future work, we will exploit the scale-similarity of the particle fields in the development of sub-grid scale

models for LES: With filter-effective and targeted Stokes numbers easily calculable, we envision LES modeling approaches (similar to the thickened flame model for LES of turbulent premixed combustion<sup>34</sup>), where the reconstruction of the missing sub-grid structure is not attempted but accounted for through corrections, e.g., to the effective collision, evaporation or condensation rates, which depend on  $St$  and  $St_{\text{eff}}$ .

### Appendix: Backtracked trajectories

Here, we provide additional 3D visualizations of sling events in order to illustrate the back- and forward tracking that was used to produce Figs. 8 and 10. Figures 12(a,b) show the trajectories of particles that engage in sling events at  $t_c = 0.6$  (FDNS1) and  $t_c = 0.4$  (FDNS5), respectively. The trajectories were obtained by tracking an ensemble of sling particles backward and forward in time from  $t = t_c$ . The color shows the fluctuation of local  $R$  that is required for the sling event. Finally, we observe that at small Stokes number, the particles retain the form of a thin sheet after the sling event has taken place, whereas a pocket forms for  $St_{\text{eff}} = 0.98$ , due to higher relative velocities.

### ACKNOWLEDGMENTS

This work was funded by the Swiss National Science Foundation under grant 200021.204621. Numerical simulations were carried out using the resources provided by

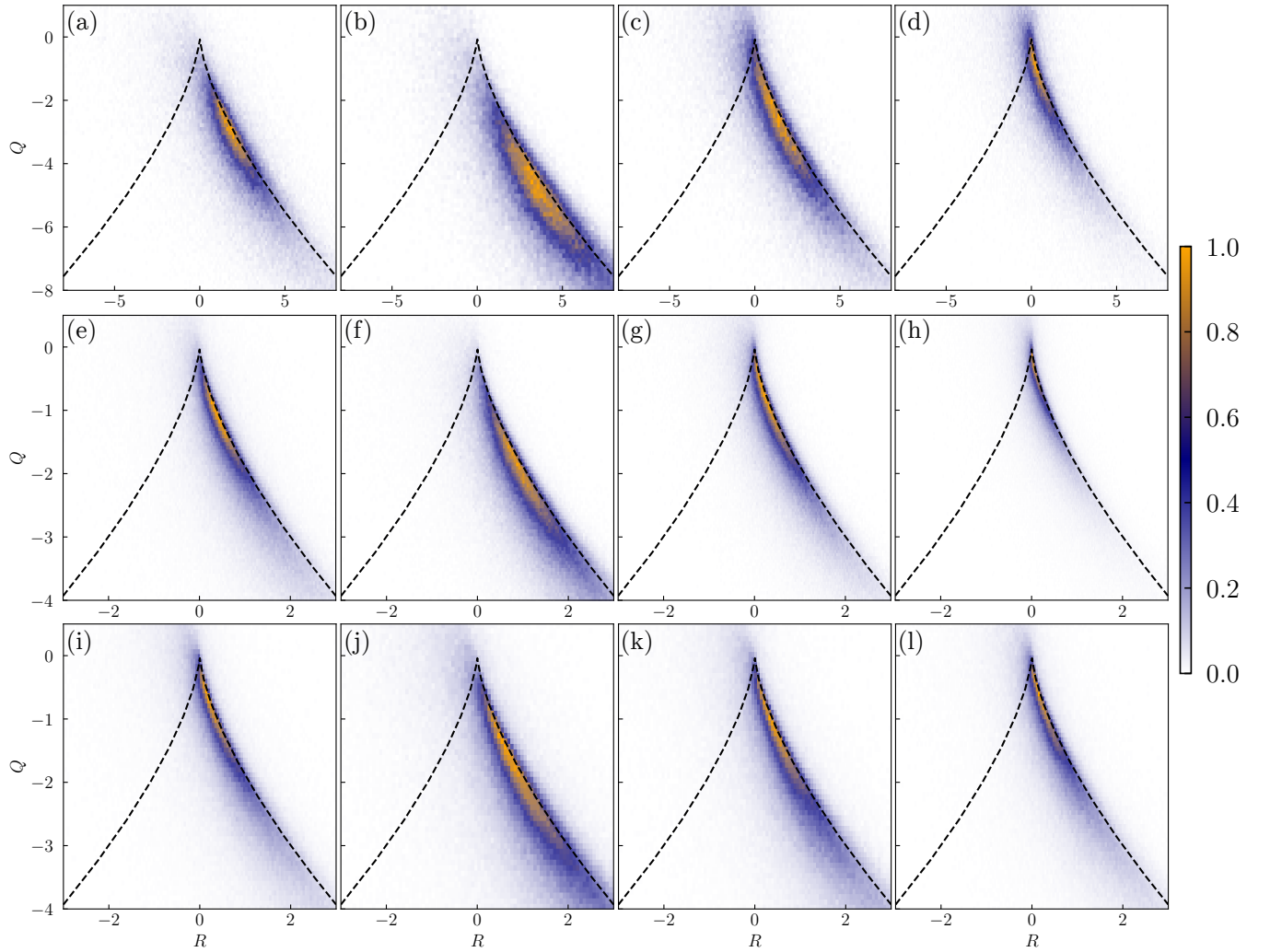


**FIG. 11:** Joint probability of  $Q$  and  $R$  along particles trajectories of the (a-d) DNS0.2, (e-h) DNS1 and (i-l) DNS5 cases, scaled by the maximum value at each time step. Time series: (a-d) and (e-h)  $t = [0.08, 0.1, 0.12, 0.14]$ , (i-h)  $t = [0, 0.04, 0.08, 0.1]$ . The vertical and horizontal axes are scaled with  $A_0$  and  $A_0^{-3/2}$ , respectively, where  $A_0$  is an arbitrary constant, (like in Fig. 2), however panels (e-l) show smaller regions of the  $QR$ -plane. The dashed black line depicts the Vieillefosse line.

the *Euler* cluster of ETH Zürich<sup>35</sup>. We thank Heinrich Heinzer for his support.

<sup>1</sup>W. W. Grabowski and L.-P. Wang, “Growth of Cloud Droplets in a Turbulent Environment,” *Annual Review of Fluid Mechanics* **45**, 293–324 (2013).

<sup>2</sup>J. Bec, “Fractal clustering of inertial particles in random flows,” *Physics of Fluids* **15**, L81–L84 (2003).

<sup>3</sup>M. R. Maxey, “The gravitational settling of aerosol particles in homogeneous turbulence and random flow fields,” *Journal of Fluid Mechanics* **174**, 441–465 (1987).

<sup>4</sup>K. D. Squires and J. K. Eaton, “Preferential concentration of particles by turbulence,” *Physics of Fluids A: Fluid Dynamics* **3**, 1169–1178 (1991).

<sup>5</sup>G. Falkovich, A. Fouxon, and M. G. Stepanov, “Acceleration of rain initiation by cloud turbulence,” *Nature* **419**, 151–154 (2002).

<sup>6</sup>M. Wilkinson and B. Mehlig, “Caustics in turbulent aerosols,” *Europhysics Letters (EPL)* **71**, 186–192 (2005).

<sup>7</sup>K. Gustavsson and B. Mehlig, “Statistical models for spatial patterns of heavy particles in turbulence,” *Advances in Physics* **65**, 1–57 (2016).

<sup>8</sup>M. Wilkinson, B. Mehlig, and V. Bezuglyy, “Caustic Activation of Rain Showers,” *Physical Review Letters* **97**, 048501 (2006).

<sup>9</sup>A. Pumir and M. Wilkinson, “Collisional Aggregation Due to Turbulence,” *Annual Review of Condensed Matter Physics* **7**, 141–170 (2016).

<sup>10</sup>P. Deepu, S. Ravichandran, and R. Govindarajan, “Caustics-induced coalescence of small droplets near a vortex,” *Physical Review Fluids* **2**, 024305 (2017).

<sup>11</sup>M. Cencini, J. Bec, L. Biferale, G. Boffetta, A. Celani, A. S. Lanotte, S. Musacchio, and F. Toschi, “Dynamics and statistics of heavy particles in turbulent flows,” *Journal of Turbulence* **7**, N36 (2006).

<sup>12</sup>J. Bec, L. Biferale, M. Cencini, A. Lanotte, S. Musacchio, and F. Toschi, “Heavy Particle Concentration in Turbulence at Dissipative and Inertial Scales,” *Physical Review Letters* **98**, 084502 (2007).

<sup>13</sup>B. Ray and L. R. Collins, “Preferential concentration and relative velocity statistics of inertial particles in Navier–Stokes turbulence with and without filtering,” *Journal of Fluid Mechanics* **680**, 488–510 (2011).



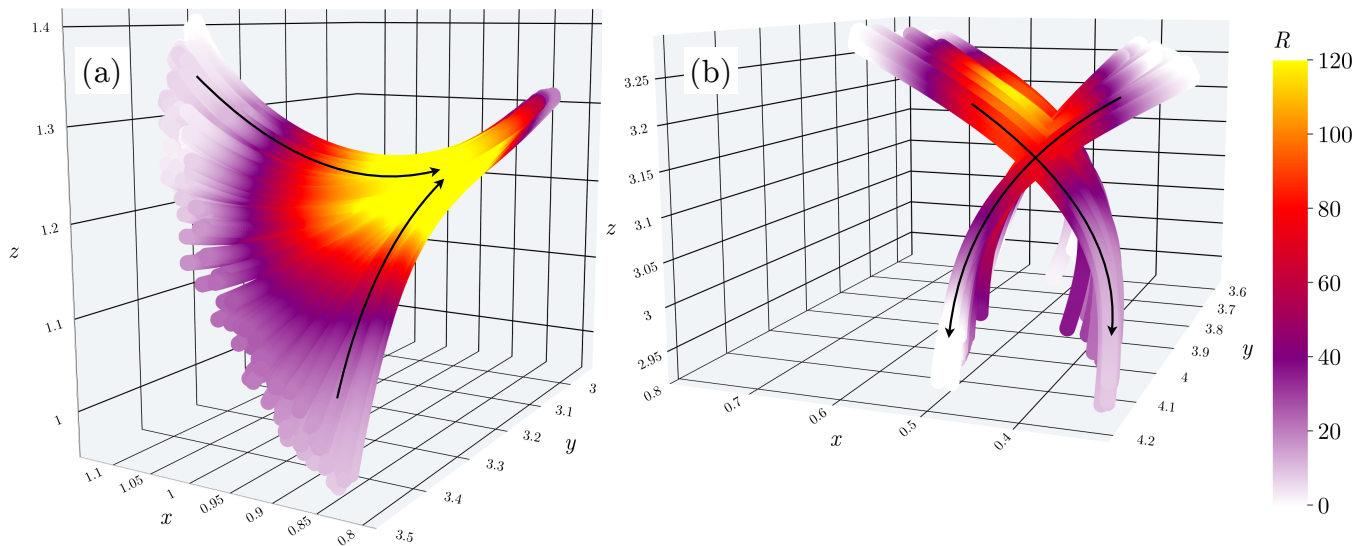


**FIG. 12:** Trajectories of (a) FDNS1 and (b) FDNS5 sling particles. The ensemble was selected using the criterion  $D > D_c$  at  $t_c = 0.6$  and  $t_c = 0.4$ , respectively, and then tracked backward (and forward) in time to create the ranges  $t \in [t_c - 0.4, t_c]$  and  $t \in [t_c - 0.4, t_c + 0.1]$ . The colors depict the locally experienced value of  $R$ . The direction of the particle motion is denoted by arrows.

- <sup>14</sup>P. L. Johnson and M. Wilczek, “Multiscale Velocity Gradients in Turbulence,” *Annual Review of Fluid Mechanics* **56**, 463–490 (2024).
- <sup>15</sup>C. Meneveau, “Lagrangian Dynamics and Models of the Velocity Gradient Tensor in Turbulent Flows,” *Annual Review of Fluid Mechanics* **43**, 219–245 (2011).
- <sup>16</sup>J. Bec, “Multifractal concentrations of inertial particles in smooth random flows,” *Journal of Fluid Mechanics* **528**, 255–277 (2005).
- <sup>17</sup>J. Bec, K. Gustavsson, and B. Mehlig, “Statistical Models for the Dynamics of Heavy Particles in Turbulence,” *Annual Review of Fluid Mechanics* **56**, 189–213 (2024).
- <sup>18</sup>J. Meibohm, V. Pandey, A. Bhatnagar, K. Gustavsson, D. Mitra, P. Perlekar, and B. Mehlig, “Paths to caustic formation in turbulent aerosols,” *Physical Review Fluids* **6**, L062302 (2021).
- <sup>19</sup>J. Meibohm, K. Gustavsson, and B. Mehlig, “Caustics in turbulent aerosols form along the Vieillefosse line at weak particle inertia,” *Physical Review Fluids* **8**, 024305 (2023).
- <sup>20</sup>J. Meibohm, L. Sundberg, B. Mehlig, and K. Gustavsson, “Caustic formation in a non-Gaussian model for turbulent aerosols,” *Physical Review Fluids* **9**, 024302 (2024).
- <sup>21</sup>R. Barta and J. Vollmer, “Caustics in turbulent aerosols: An excitable system approach,” *Journal of Fluid Mechanics* **949**, A36 (2022).
- <sup>22</sup>A. Bhatnagar, V. Pandey, P. Perlekar, and D. Mitra, “Rate of formation of caustics in heavy particles advected by turbulence,” *Philosophical Transactions of the Royal Society A: Mathematical, Physical and Engineering Sciences* **380**, 20210086 (2022).
- <sup>23</sup>S. Lee and C. Lee, “Identification of a particle collision as a finite-time blowup in turbulence,” *Scientific Reports* **13**, 181 (2023).
- <sup>24</sup>J. Meibohm and B. Mehlig, “Heavy particles in a persistent random flow with traps,” *Physical Review E* **100**, 023102 (2019).
- <sup>25</sup>P. Vieillefosse, “Local interaction between vorticity and shear in a perfect incompressible fluid,” *Journal de Physique* **43**, 837–842 (1982).
- <sup>26</sup>Y. Li, E. Perlman, M. Wan, Y. Yang, C. Meneveau, R. Burns, S. Chen, A. Szalay, and G. Eyink, “A public turbulence database cluster and applications to study Lagrangian evolution of velocity increments in turbulence,” *Journal of Turbulence* **9**, N31 (2008).
- <sup>27</sup>P. Jenny, M. Torrilhon, and S. Heinz, “A solution algorithm for the fluid dynamic equations based on a stochastic model for molecular motion,” *Journal of Computational Physics* **229**, 1077–1098 (2010).
- <sup>28</sup>P. J. Ireland, T. Vaithianathan, P. S. Sukheswalla, B. Ray, and L. R. Collins, “Highly parallel particle-laden flow solver for turbulence research,” *Computers & Fluids* **76**, 170–177 (2013).
- <sup>29</sup>S. B. Pope, *Turbulent Flows* (Cambridge University Press, 2000).
- <sup>30</sup>S. Goto and J. C. Vassilicos, “Self-similar clustering of inertial particles and zero-acceleration points in fully developed two-dimensional turbulence,” *Physics of Fluids* **18**, 115103 (2006).
- <sup>31</sup>X. Wang, M. Wan, Y. Yang, L.-P. Wang, and S. Chen, “Reynolds number dependence of heavy particles clustering in homogeneous isotropic turbulence,” *Physical Review Fluids* **5**, 124603 (2020).
- <sup>32</sup>G. P. Bewley, E.-W. Saw, and E. Bodenschatz, “Observation of the sling effect,” *New Journal of Physics* **15**, 083051 (2013).
- <sup>33</sup>I. Fouxon, S. Lee, and C. Lee, “Intermittency and collisions of fast sedimenting droplets in turbulence,” *Physical Review Fluids* **7**, 124303 (2022).
- <sup>34</sup>O. Colin, F. Ducros, D. Veynante, and T. Poinot, “A thickened flame model for large eddy simulations of turbulent premixed combustion,” *Physics of Fluids* **12**, 1843–1863 (2000).
- <sup>35</sup>ETH Zürich, “Euler,” <https://scicomp.ethz.ch/wiki/Euler>.